ACS OMEGA

http://pubs.acs.org/journal/acsodf

Article

Biologically Synthesized *Rosa rugosa*-Based Gold Nanoparticles Suppress Skin Inflammatory Responses via MAPK and NF-κB Signaling Pathway in TNF-α/IFN-γ-Induced HaCaT Keratinocytes

Rongbo Wang, Sung-Kwon Moon, Woo-Jung Kim, Sanjeevram Dhandapani, Hoon Kim,* and Yeon-Ju Kim*

Cite This: *ACS Omega* 2022, 7, 35951−35960

Read Online

ACCESS | Metrics & More | Article Recommendations | Supporting Information

ABSTRACT: Nanotechnology-applied materials and related therapeutics have gained attention for treating inflammatory skin diseases. The beach rose (*Rosa rugosa*), belonging to the family Rosaceae, is a perennial, deciduous woody shrub endemic to northeastern Asia. In this study, *R. rugosa*-based gold nanoparticles (RR-AuNPs) were biologically synthesized under optimal conditions to explore their potential as anti-inflammatory agents for treating skin inflammation. The synthesized RR-AuNPs were analyzed using field emission-transmission electron microscopy, energy-dispersive X-ray spectrometry, selected-area electron diffraction, and X-ray diffraction. The uniformly well-structured AuNPs showed near-spherical and polygonal shapes. Cell viability evaluation and optical observation results showed that the RR-AuNPs were absorbed by human keratinocytes without causing cytotoxic effects. The effects of RR-AuNPs on the skin inflammatory response were investigated in human keratinocytes treated with tumor necrosis factor-α/interferon-γ (T + I). The results showed that T + I-stimulated increases in inflammatory mediators, including chemokines, interleukins, and reactive oxygen species, were significantly suppressed by RR-AuNP treatment in a concentration-dependent manner. The western blotting results indicated that the RR-AuNP-mediated anti-inflammatory effects were highly associated with the suppression of inflammatory signaling, mitogen-activated protein kinase, and nuclear factor-κB. These results demonstrate that plant extract-based AuNPs are novel anti-inflammatory candidates for topical application to treat skin inflammation.

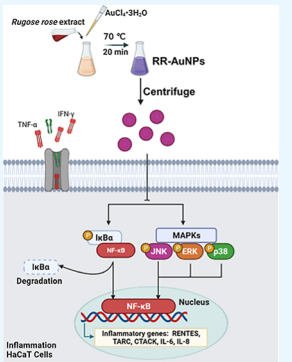

1. INTRODUCTION

In addition to its many crucial roles, such as storing lipids and water, creating sensation, preventing water and nutrient losses, and controlling body temperature, the skin is an important part of the immune system responsible for the primary defense against various external stimuli and for maintaining tissue homeostasis.[1,2] However, abnormal or uncontrolled immune responses in the skin tissue induce skin inflammation.[3] Moreover, persistent and pathological inflammatory responses in the skin tissue contribute to the development of inflammatory skin disease (ISD), which is known as dermatitis and includes atopic, allergic, contact, seborrheic, and stasis dermatitis.[4,5] Particularly, atopic dermatitis is a chronic intractable ISD characterized by eczema, itching (pruritus), redness, lichenification, cracking, and infection.[6] As ISDs are increasing worldwide because of rapid industrialization and environmental pollution, several medications, including topical steroid ointments, oral antihistamines, phototherapy, immunomodulators, and antibiotics, have been used to treat ISDs.[7] However, long-term use of these agents is associated with serious side effects, such as skin thinning, atrophy, fragility, ecchymosis, poor wound healing, vascular expansion, and hormone dysfunction.[8] Therefore, a new approach for developing alternative medications to treat ISDs is urgently required.

Recent studies suggested that nanotechnology can be used to prevent and treat inflammatory diseases. Various nano-sized materials, particularly nanoparticles, have been studied to determine their roles in inflammatory responses.[9,10] These materials can improve bioavailability and drug delivery at the inflammation site while causing few side effects and have a good safety profile.[11] Several researchers have proposed using nanoparticles, such as polymeric nanoparticles, metallic nanoparticles, lipid nanoparticles, and vesicular systems, because of their stable, safe, and target-specific delivery characteristics for treating numerous disorders.[12,13] In recent years, plant-based metallic nanoparticles produced using green synthesis methods have been explored to optimize the conventional efficacy of the original plants based on their advantages, including their high biocompatibility, low cost, and eco-friendly nature.[14−16] Nevertheless, further research on metallic nanoparticles synthesized

Received: July 30, 2022
Accepted: September 8, 2022
Published: September 30, 2022

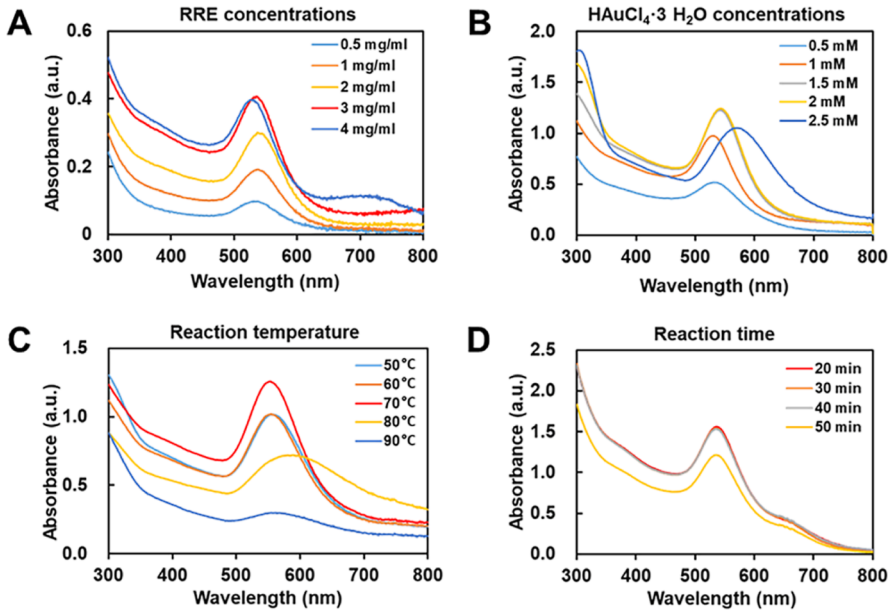

Figure 1. Reaction condition-dependent evolution of UV−vis spectra of synthesized nanoparticles to maximize the nanoparticle yield. (A) Concentration of *R. rugosa* extract (RRE); (B) concentration of $HAuCl_4 \cdot 3H_2O$; (C) reaction temperature; and (D) reaction time of UV−vis spectra of gold nanoparticles (RR-AuNPs) synthesized from RRE.

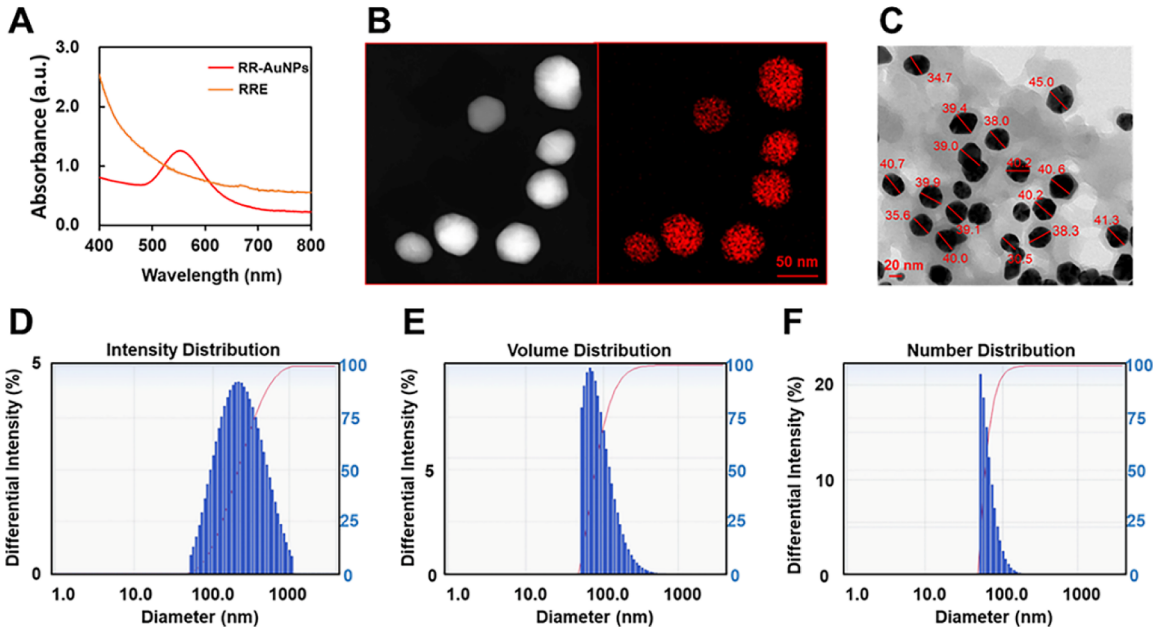

Figure 2. Physical properties of gold nanoparticles (RR-AuNPs) synthesized from *R. rugosa* extract (RRE). (A) UV−vis spectrum of RR-AuNPs and RRE; (B) elemental mapping; (C) FE-TEM image of RR-AuNPs; DLS analysis of (D) intensity, (E) volume, and (F) number distributions of RR-AuNPs.

from various types of plants is needed to develop anti-inflammatory candidates.

The beach rose (*Rosa rugosa*, RR), belonging to the family Rosaceae, is a perennial, deciduous woody shrub endemic to northeastern Asia, including Korea, China, and Japan.[17] Beyond its traditional use in ornamentals and aromatics, RR exhibits several pharmacological effects, such as antioxidative,[18,19] anti-inflammatory,[20] anticancer,[21] and antihypertensive[22] effects. In a nanonization study, Dubey et al. synthesized silver and gold nanoparticles (AuNPs) with mean particle sizes of 12 and 11 nm, respectively, using RR leaf tissue.[23] However, only the synthesis conditions and physiochemical characteristics of the nanoparticles were evaluated, without considering any pharmacological properties. Therefore, the physiological and medicinal characteristics of RR-based nanoparticles should be investigated. This study was conducted to prepare novel AuNPs using RR extracts and identify their physicochemical characteristics. In addition, we examined the effect of RR-based AuNPs (RR-AuNPs) on inflammatory responses in the skin and underlying molecular mechanisms in an inflammation-induced human keratinocyte model.

https://doi.org/10.1021/acsomega.2c04832
ACS Omega 2022, 7, 35951−35960

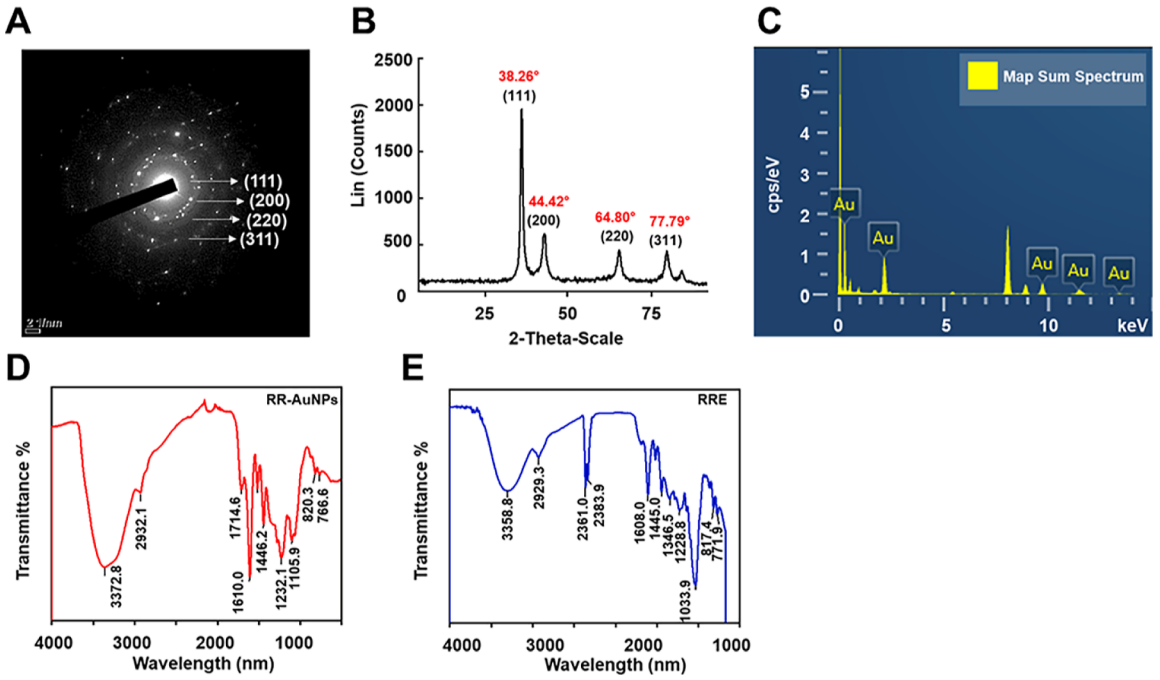

Figure 3. Chemical characteristics of gold nanoparticles (RR-AuNPs) synthesized from *R. rugosa* extract (RRE). (A) SAED image of RR-AuNPs; (B) XRD spectrum of RR-AuNPs; (C) EDS of RR-AuNPs; FT-IR spectrum of (D) RR-AuNPs and (E) RRE.

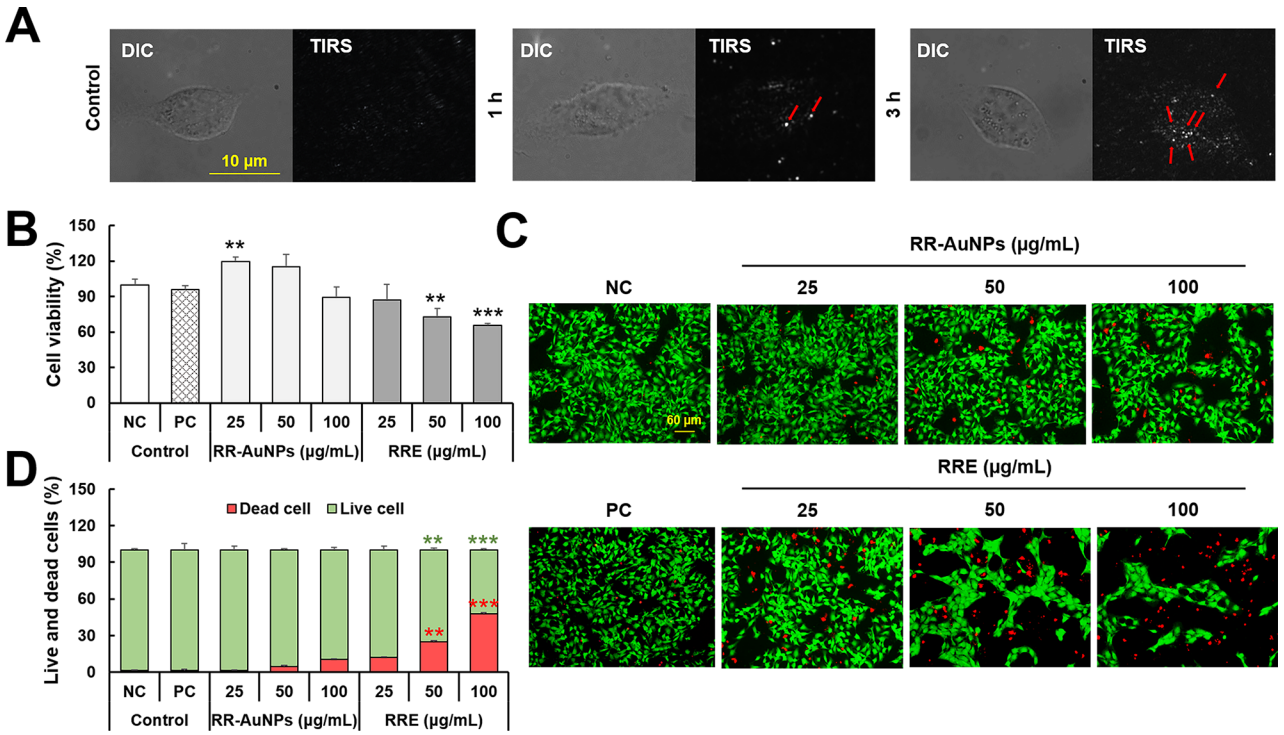

Figure 4. Intercellular uptake and cytotoxic effect of RR-AuNPs. (A) DIC and TIRS microscopic images of the cellular uptake of RR-AuNPs in HaCaT cells. (B) Cytotoxic effect of RR-AuNPs against HaCaT cells obtained by MTT method. (C) Fluorescence images and their (D) quantified results of HaCaT cells treated with RR-AuNPs and RRE, following staining with live/dead cell staining dye. NC, negative control treated with medium alone; PC, positive control treated with dexamethasone (20 μg/mL). Arrows indicate the RR-AuNPs accumulated inside HaCaT cells after treatment. Asterisks indicate significant differences between NC and each group. *$p < 0.05$, **$p < 0.01$, ***$p < 0.001$.

2. RESULTS

2.1. Biosynthesis and Physiochemical Characterization of RR-AuNPs. To establish the optimal biosynthesis conditions, several reaction parameters, including the extract of RR (RRE) concentrations (0.5−4 mg/mL), gold salt concentrations (0.5−2.5 mM), reaction temperatures (50−90 °C), and times (20−50 min), were monitored using ultraviolet−visible (UV−vis) spectrophotometry (Figure 1). The optimal conditions for RR-AuNPs biosynthesis were 3 mg/mL RRE and 2 mM gold salt incubated at 70 °C for 20 min. RR-AuNPs

https://doi.org/10.1021/acsomega.2c04832
ACS Omega 2022, 7, 35951−35960

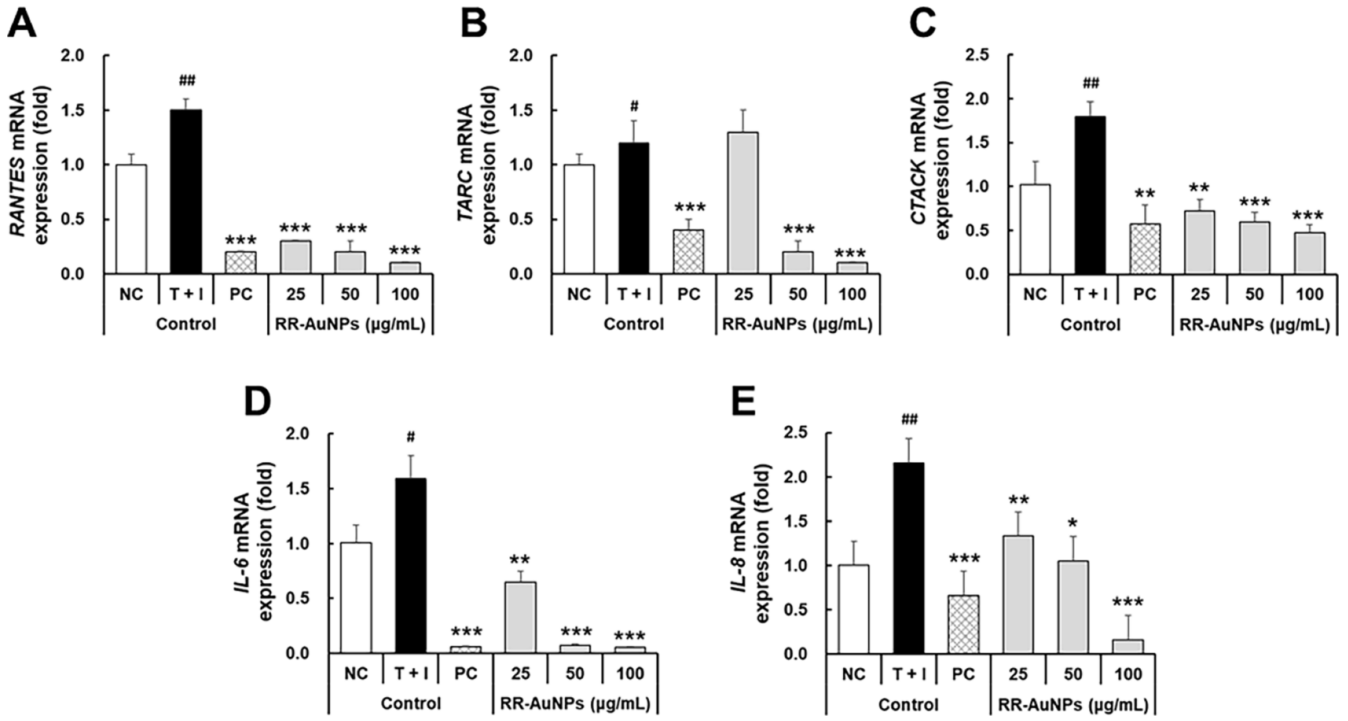

Figure 5. Effects of RR-AuNPs on mRNA expression in TNF-α/IFN-γ (T + I)-induced HaCaT cells. A qRT-PCR assay was conducted to measure the mRNA expression of (A) *RENTES*, (B) *TARC*, (C) *CTACK*, (D) *IL-6*, and (E) *IL-8*. NC treated with medium alone; T + I, inflammation-induced control treated with T + I alone; PC treated with dexamethasone followed by T + I stimulation. The crosshatch marks indicate significant differences between NC and T + I, and asterisks indicate significant differences between T + I and each group. $^{\#}$ and $^{*}p < 0.05$; $^{\#\#}$ and $^{**}p < 0.01$; $^{***}p < 0.001$.

synthesized under optimal conditions had an λ_{max} of 545 nm, whereas RRE and gold salts alone showed no plasmonic absorbance (Figure 2A). The stability of RR-AuNPs is presented in Figure S1. The result reveals that RR-AuNPs were quite stable at room temperature for 30 days after synthesis. Elemental mapping revealed that gold elements (red dots) were uniformly distributed within the nanoparticles, indicating that RR-AuNPs were synthesized into AuNPs without impurities (Figure 2B). The morphological and structural features of RR-AuNPs were observed using a field emission transmission electron microscope. The TEM images showed that RR-AuNPs had predominantly near-spherical and polygonal shapes with a mean diameter of 38.2 ± 3.7 nm (Figure 2C). From the dynamic light scattering (DLS) analysis, we were able to obtain the hydrodynamic size of the nanoparticles. DLS particle analysis revealed that average intensity, volume, and number distributions of RR-AuNPs were 293.0, 104.1, and 72.1 nm, respectively (Figure 2D−F). The crystallographic techniques selected area electron diffraction (SAED) and X-ray diffraction (XRD) were used to identify the crystalline nature of the RR-AuNPs. Four rings (111, 200, 220, and 311) were observed in the crystalline plane of the SAED pattern (Figure 3A) in addition to four diffraction peaks at θ values of 38.26, 44.42, 64.80, and 77.79° [corresponding to the (111), (200), (220), and (300) planes, respectively] shown in the XRD spectrum (Figure 3B), indicating that the RR-AuNPs had a face-centered cubic crystalline structure. Figure 3C shows the high density of the Au peak in the energy-dispersive spectroscopy (EDS) spectrum, indicating that gold was the predominant element in the RR-AuNPs. Additional signals originating from copper were also found in the EDX spectrum because of the use of the grid in EDX analysis. Fourier transform infrared spectroscopy (FT-IR) was performed to identify and compare the surface functional groups of RR-AuNPs and RRE (Figure 3D,E, respectively). The two samples exhibited different absorption patterns. According to the spectral library, the bands observed at 3372.8 and 3358.8 cm^{-1} in RR-AuNPs and RRE, respectively, are assigned to the phenolic hydroxyl and aliphatic hydroxyl groups.[24] The bands observed at 2932.1 cm^{-1} in RR-AuNPs and 2929.3 cm^{-1} in RRE are associated with the C−H stretch of the methylene groups of the protein.[25] The sharp signals from 2361.0 and 2338.9 cm^{-1} in the RRE correspond to C−H stretching,[26] whereas this peak was faded in the AuNPs. The band at 1714.6 cm^{-1} for the RR-AuNPs is characteristic of the stretching C═O group. The peaks at 1610.6 cm^{-1} in RR-AuNPs and the peak at 1608.0 cm^{-1} in RRE may be due to the presence of C═C of benzene.[27] The signals at 1446.2, 1232.1, and 1105.9 cm^{-1} in RR-AuNPs and signals at 1445.0, 1346.5, 1228.8, and 1033.9 cm^{-1} in RRE correspond to the C−H bending vibration, which arises from alkenes[28] and aliphatic amine functional groups. These results indicate that the functional groups of RRE were modified by interactions with the gold salts. The results of FT-IR analysis strongly supported that capping of RRE endowed the synthesized RR-AuNPs with high stability.

2.2. Intercellular Uptake and Cytotoxic Effect of RR-AuNPs. Figure 4A shows the total internal reflection scattering (TIRS) microscopy system equipped with differential interference contrast (DIC) images of the RR-AuNPs. As shown in the TIRS image, bright light was generated inside the cells at 1 h after RR-AuNP treatment. At 3 h after treatment, more light was accumulated inside the cells. These results revealed that RR-AuNPs were absorbed by HaCaT cells in a time-dependent manner. A cytotoxicity test was performed to confirm the safety of the RR-AuNPs and RRE. HaCaT cells were treated with equivalent concentrations of RR-AuNPs and RRE for 24 h, and then a conventional 3-(4, 5-dimethylthiazol-2-yl)-2,5-diphenyl-

https://doi.org/10.1021/acsomega.2c04832
ACS Omega 2022, 7, 35951−35960

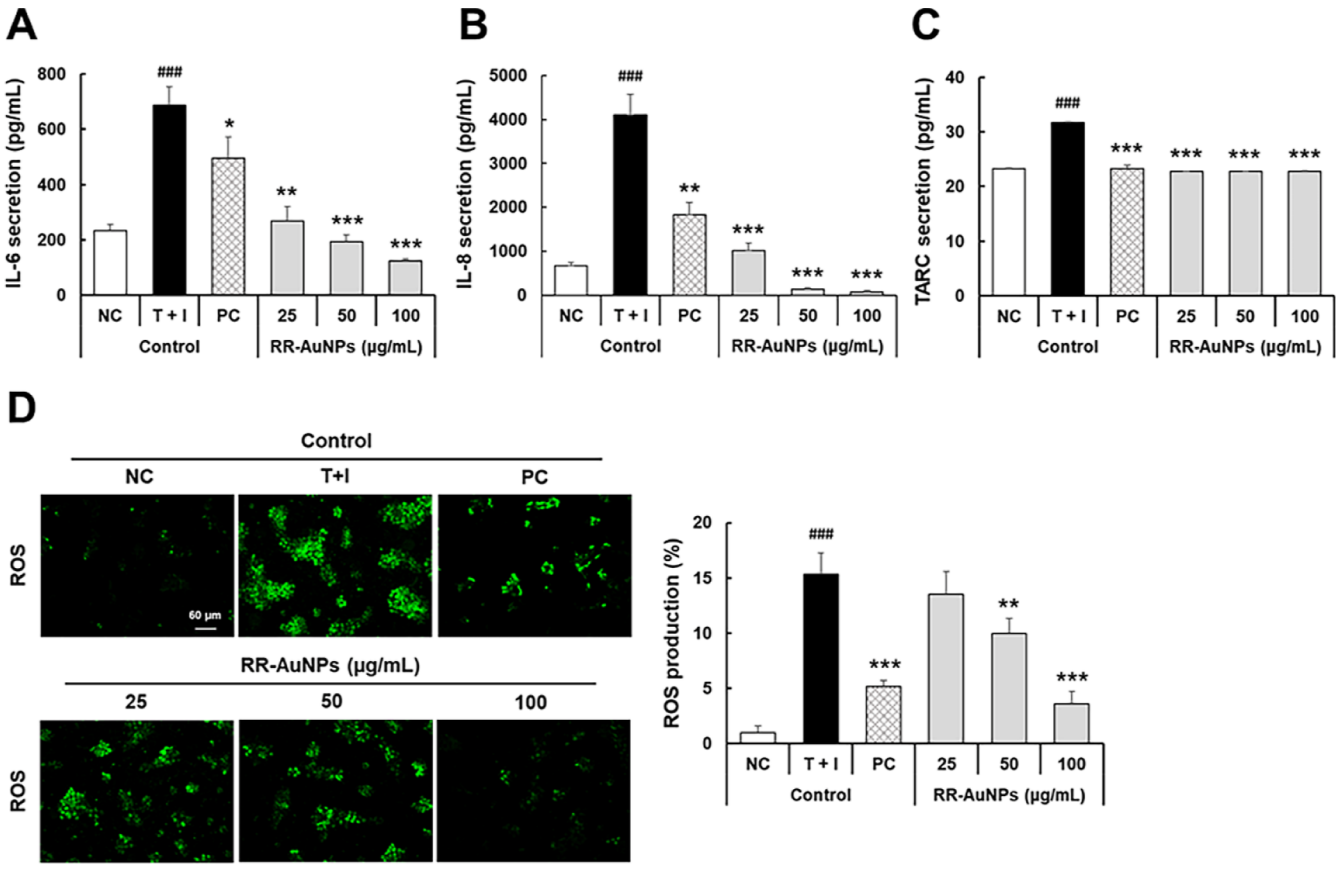

Figure 6. Effect of RR-AuNPs on the production of inflammatory cytokines and ROS in TNF-α/IFN-γ (T + I)-stimulated HaCaT cells. The production of (A) IL-6, (B) IL-8, and (C) TARC was measured using ELISA of the culture supernatant of T + I-stimulated HaCaT cells. (D) Fluorescence images and quantification of the results from HaCaT cells treated with RR-AuNPs, following staining with ROS staining dye. NC treated with medium alone; T + I, inflammation-induced control treated with T + I alone; PC treated with dexamethasone followed by T + I stimulation. The crosshatch marks indicate significant differences between NC and T + I, and asterisks indicate significant differences between T + I and each group. *p < 0.05; **p < 0.01; ### and ***p < 0.001.

tetrazolium bromide (MTT) assay and live/dead cell staining were performed. The MTT assay revealed that RR-AuNPs were not significantly cytotoxic at any of the concentrations tested (25−100 μg/mL), whereas RRE exhibited a significant toxic effect at concentrations above 50 μg/mL (Figure 4B). Figure 4C shows a representative image of cells stained with live/dead cell-staining dye, and the quantified results are shown in Figure 4D. The results revealed no significant accumulation of red dots in RR-AuNP-treated cells at all concentrations tested, but the viability of cells treated with RRE at 50 and 100 μg/mL was significantly reduced.

2.3. Inhibitory Effects of RR-AuNPs on T + I-Induced Inflammation and Oxidative Stress in HaCaT Cells. To establish an *in vitro* skin inflammation model, HaCaT cells were stimulated with T + I. As shown in Figure 5, the qRT-PCR results showed that the gene expression levels of pro-inflammatory chemokines, such as primarily CC motif chemokine ligands (*CCLs*), including CCL5/regulated upon activation, normal T cell expressed and presumably secreted (*RANTES*), CCL17/thymus and activation-regulated chemokine (*CCL17/TARC*), CCL27/cutaneous T cell-attracting chemokine (*CCL27/CTACK*), CXC motif chemokine ligand 8 (CXCL8)/interleukin 8 (*IL-8*), and interleukin 6 (*IL-6*), were significantly upregulated in T + I-treated cells. RR-AuNP treatment significantly decreased the expression of these genes in a concentration-dependent manner. Particularly, RR-AuNP treatment at a high concentration (100 μg/mL) led to greater downregulation of these genes compared to that induced by dexamethasone treatment, which was used as a PC. To verify the inhibitory effects of RR-AuNPs, the secretory levels of IL-6, IL-8, and TARC proteins in the cell culture supernatant were determined using enzyme-linked immunosorbent assay (ELISA). As shown in Figure 6A−C, T + I-induced increases in IL-6, IL-8, and TARC were concentration-dependently decreased by RR-AuNP treatment. Interestingly, RR-AuNP treatment at all concentrations tested exhibited higher inhibitory effects on the three inflammatory mediators than in the PC group. These results demonstrate that RR-AuNPs effectively inhibited skin inflammation-associated mediators at the gene expression and protein secretion levels. Next, we investigated intracellular reactive oxygen species (ROS) production in T + I-induced HaCaT cells. Figure 6D shows representative images of cells stained with ROS staining dye, along with the quantified results. The results showed that HaCaT cells produced excessive intracellular ROS following T + I stimulation alone, and RR-AuNPs significantly decreased the production of toxic biomarkers in a dose-dependent manner. Specifically, cells treated with RR-AuNPs at a high concentration (100 μg/mL) showed higher ROS inhibitory effects compared to those in the PC group. This result suggests that RR-AuNP-induced suppression of intracellular oxidative stress is associated with anti-inflammatory responses in skin cells.

https://doi.org/10.1021/acsomega.2c04832
ACS Omega 2022, 7, 35951−35960

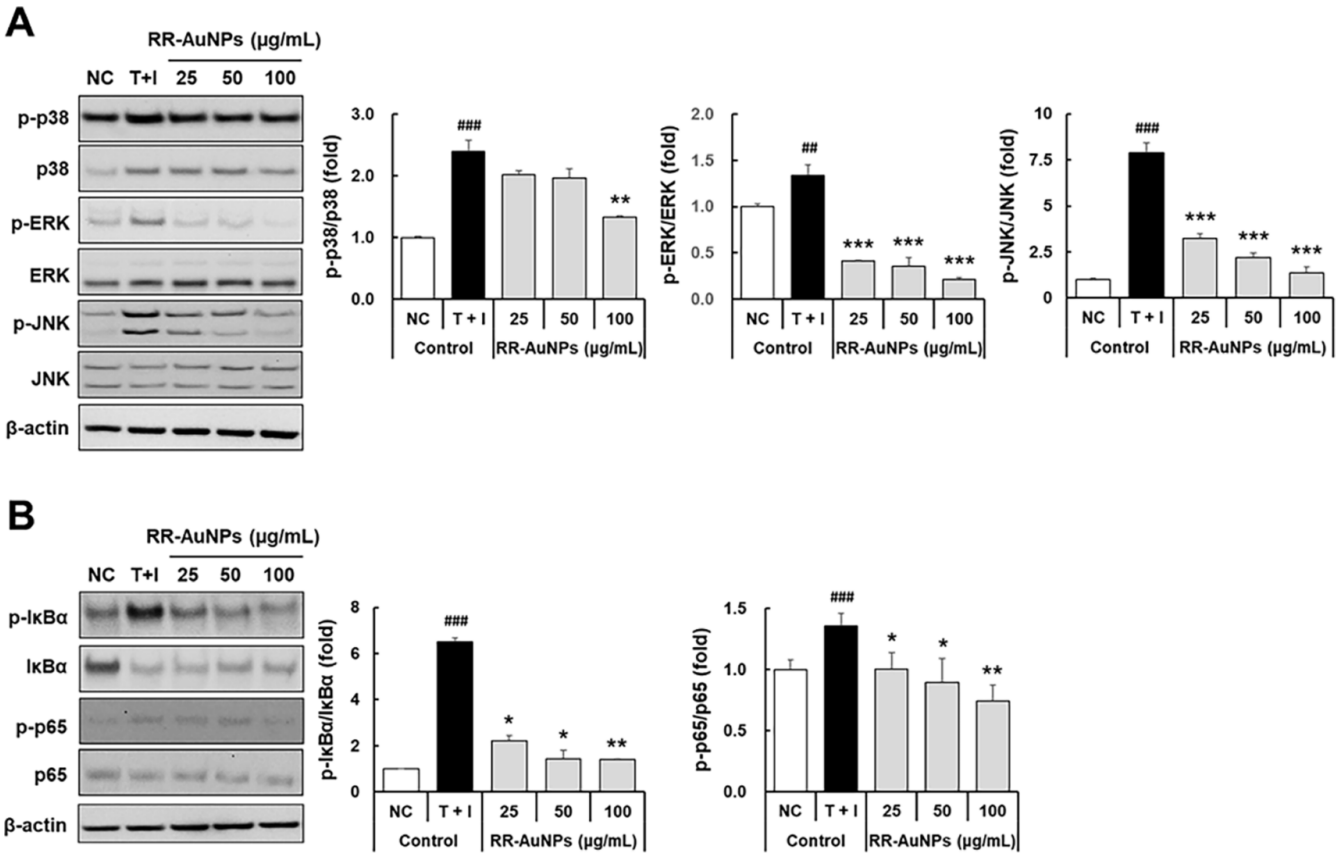

Figure 7. Effect of RR-AuNPs on (A) MAPK and (B) nuclear factor (NF)-κB in TNF-α/IFN-γ (T + I)-stimulated HaCaT cells. The expression or phosphorylation of the indicated proteins was determined in whole-cell lysates by western blotting using the indicated antibodies. NC treated with medium alone; T + I, inflammation-induced control treated with T + I alone. Crosshatch marks indicate significant differences between NC and T + I, and asterisks indicate significant differences between T + I and each group. *$p < 0.05$; ## and **$p < 0.01$; ### and ***$p < 0.001$.

2.4. Inhibitory Mechanism of Action on the Skin Inflammatory Response. To identify the intracellular mechanism underlying RR-AuNP-induced inhibition of the skin inflammatory response, mitogen-activated protein kinase (MAPK) (Figure 7A) and nuclear factor kappa-light-chain-enhancer of activated B cells (NF-κB) (Figure 7B) were evaluated using western blotting. In HaCaT cells, T + I stimulation significantly elevated the phosphorylated levels of three MAPKs (p38 kinase, ERK, and JNK) but did not alter their total levels. The T + I-induced increase in phosphorylated MAPKs was downregulated by RR-AuNP treatment in a concentration-dependent manner. Similar tendencies were observed for NF-κB p65. However, T + I treatment significantly upregulated the phosphorylation level of IκBα and markedly downregulated the total protein level. The increased expression of p-IκBα by T + I stimulation was significantly downregulated by RR-AuNP treatment in a concentration-dependent manner. These findings indicate that T + I-induced skin inflammation was markedly suppressed by RR-AuNP treatment *via* the MAPK and NF-κB pathways.

3. DISCUSSION

We explored the biosynthesis, characteristics, and anti-inflammatory activities of RR-AuNPs to investigate their potential for industrial application as anti-inflammatory agents. First, monitoring of various synthetic conditions of the nanoparticles showed that RR-AuNPs were successfully synthesized under optimal conditions (Figure 1). The synthesized RR-AuNPs were uniformly well-structured with near-spherical and polygonal shapes. Interestingly, the particle sizes of the RR-AuNPs differed (Figure 2C−F, respectively), possibly because of the difference in the analytical principles between different analyses. The intensity weighted distribution shows how different-size particles are detected from a fit to the autocorrelation function of the measured scattering. Based on the intensity, results can therefore be highly sensitive to very small numbers of aggregates or dust. The number and volume distribution show the relative proportion of the number of different-size particles and the volume occupied by different-size particles. As DLS analysis reveals the nanoparticle size based on the whole size of the conjugates or their hydrodynamic size in the colloids, the obtained sizes are generally noticeably larger than those obtained using TEM analysis.[25] The structure and conformation of the surface functional groups of RR-AuNPs were coordinated compared with those of RRE (Figure 3D,E).[29,30] In 2010, Dubey et al.[23] reported that the biologically synthesized AuNPs have mostly hexagonal shapes and a mean size of 11 nm. Compared with RR-AuNPs (mean size of 38.2 nm), the smaller size of their AuNPs may have resulted from the shorter synthesis time (10 min).

RR-AuNPs were absorbed into the HaCaTs without causing cytotoxic effects (Figure 4A). Compared with the cytotoxic effect induced by RRE, RR-AuNPs may be safer, although they act inside the cells following absorption. Next, the anti-dermatitis effect of RR-AuNPs was evaluated using T + I-stimulated HaCaT cells. Many previous studies have demon-

https://doi.org/10.1021/acsomega.2c04832
ACS Omega 2022, 7, 35951−35960

strated that the pathogenesis of ISDs is triggered and motivated by keratinocyte-secreting chemokines, including CCL5/RANTES,[31] CCL17/TARC,[32] CCL22/macrophage-derived chemokine,[33] CCL27/CTACK,[34] and CXC8/IL-8,[35] which are involved in recruiting leukocytes to inflammatory skin tissue. Particularly, the inflammatory cytokines TNF-α and IFN-γ, which are mainly secreted by macrophages and T cells, can stimulate the production and secretion of inflammatory chemokines in epidermal keratinocytes.[6,36] T + I-stimulated inflammatory responses in keratinocytes are accompanied by intracellular ROS accumulation and their extracellular secretion.[37,38] In addition to the basic role of forming a physical barrier by differentiating into corneocytes to protect the body, epidermal keratinocytes trigger and induce the progression of ISDs.[39,40] Accordingly, numerous studies have applied in vitro models using T + I-induced epidermal keratinocytes to explore their potential as anti-inflammatory agents in the skin.[3,4,41,42] RR-AuNPs considerably downregulated the expression of T + I-induced inflammatory genes, including *RANTES*, *TARC*, *CTACK*, *IL-6*, and *IL-8* (Figure 5). Additionally, the secretion levels of IL-6, IL-8, and TARC proteins were significantly suppressed following pretreatment with RR-AuNPs (Figure 6A−C). These results indicate that RR-AuNPs can effectively inhibit inflammatory responses in keratinocytes. In addition, T + I-induced mitochondrial ROS production was considerably decreased by RR-AuNP treatment (Figure 6D), indicating that oxidative stress-associated damage during inflammatory responses can be alleviated by RR-AuNP treatment. T + I-stimulated inflammatory responses in keratinocytes mediate the generation of intracellular ROS, leading to the activation of inflammatory signaling cascades.[37,38]

Based on these results, we further explored the mechanism of action underlying the anti-inflammatory efficacy exerted by RR-AuNPs. MAPK and NF-κB signaling are major signaling pathways in various inflammatory responses, including skin dermatitis. In addition to its crucial function in regulating cell survival, such as differentiation, proliferation, mitosis, and death, activation of MAPK signaling contributes to the pathogenesis of diverse diseases, including chronic inflammation.[43,44] Thus, searching for substances that can regulate compromised MAPK signaling may be useful for developing targeted therapies for inflammatory disorders.[44] Three distinct MAPKs, ERK, JNK, and p38, are key targets for exploring the progression of diverse diseases.[43,45] The NF-κB signaling pathway is closely involved in the pathogenesis of ISDs.[3] The NF-κB subfamily comprises five transcription factors: NF-κB1 (p105/p50), NF-κB2 (p100/p52), RelA (p65), RelB, and c-Rel.[46,47] Under physiological conditions, the activity of NF-κB proteins is inhibited by their inhibitor proteins, including IκBα, IκBβ, and IκBγ.[47] Upon stimulation, the inactive form of the NF-κB/IκB complex in the cytoplasm is activated, followed by phosphorylation and release of IκB from the complex, translocation of NF-κB into the nucleus, and transcription initiation of inflammatory genes.[23,47] We measured the phosphorylation levels of three MAPKs (p38, ERK, and JNK) and two NF-κB signaling-related molecules (IκBα and p65) to identify the mechanism of action underlying RR-AuNP-mediated suppression of the T + I-stimulated inflammatory reaction. As shown in Figure 7, RR-AuNPs considerably suppressed the T + I-stimulated activation of MAPK and NF-κB signaling molecules. Taken together, our results demonstrate that RR-AuNPs can be taken up by keratinocytes without causing cytotoxicity and suppress the production of T + I-stimulated inflammatory mediators (chemokines, cytokines, and ROS) by downregulating both MAPK and NF-κB signaling. To the best of our knowledge, this is the first study to demonstrate the physicochemical and anti-inflammatory properties of AuNPs prepared from RR.

4. CONCLUSIONS

We biologically synthesized uniformly shaped RR-AuNPs with a mean diameter of 38.2 nm using RR (RR-AuNPs) and gold salts under optimal synthesis conditions. The synthesized RR-AuNPs were absorbed by HaCaT cells without causing significant cytotoxic effects in HaCaT cells treated with RR-AuNPs compared to in cells treated with only RRE. Thus, the cytotoxic effect of RRE may be decreased *via* its conversion into RR-AuNPs, suggesting that nanonization using green synthesis is a useful technique for decreasing its cytotoxic effect in keratinocytes. In addition, the RR-AuNPs noticeably inhibited the generation of inflammatory mediators in T + I-induced HaCaT cells; these effects were associated with the downregulation of the MAPK and NF-κB signaling pathways. Our study provides valuable preliminary results on plant extract-based AuNPs and can be utilized to develop anti-inflammatory candidates for topical application. Nevertheless, possible toxicity following long-term treatment with RR-AuNPs should be evaluated in an animal model in further studies.

5. MATERIALS AND METHODS

5.1. Harvest and Extraction of Wild RR. Branch tissue of wild RR was harvested from northern Gyeonggi, adjacent to the demilitarized zone in Korea. The plant was identified by Dr. J. K. Kim, a senior researcher at Gyeonggido Business and Science Accelerator, Gyeonggi Biocenter (Suwon, Korea). A voucher specimen was deposited in the department described above. Dried branches were extracted with five volumes (w/v) of 50% ethanol at 20−25 °C for 3 days. The extracts were filtered through a polyester filter cloth (20 μm; Hyundai Micro, Anseong, Korea) and evaporated using a rotary evaporator (Buchi Korea, Inc., Gwangmyeong, Korea) to remove the ethanol. The remaining solution was lyophilized using a freeze drier (Ilshin Biobase, Daejeon, Korea) for 3 days to yield a 50% ethanol extract of RR (RRE) with an extraction yield of 19.6%.

5.2. Synthesis and Optimization of RR AuNPs. The biosynthesized RR-AuNPs were prepared from RRE as described previously.[48] In addition, four reaction parameters were examined to optimize the biosynthesis of the RR-AuNP, including the RRE and tetrachloroauric(III) acid trihydrate (gold salts; Sigma-Aldrich, St. Louis, MO, USA) concentrations, reaction temperature, and reaction time.[48] After the reaction of RRE and the gold salts, the color change was evaluated and absorbance at 300−800 nm was determined visually and using a UV−vis spectrophotometer (Agilent Technologies, Santa Clara, CA, USA), respectively. The synthesized RR-AuNPs were centrifuged at 13,475*g* for 10 min and washed five times with deionized water along with repeated centrifugation. The purified particles were lyophilized using a freeze drier (Ilshin Biobase) to obtain powdered RR-AuNPs.

5.3. Physicochemical Characterization of RR-AuNPs. The morphological, crystallographic, and elemental characteristics of the RR-AuNPs were measured using a high-resolution transmission electron microscope (JEOL JEM-2100F, Tokyo, Japan) equipped with EDS and SAED. The purity and crystalline nature of the RR-AuNPs were measured using an XRD (Bruker, Billerica, MA, USA). The intensity, volume, and number

https://doi.org/10.1021/acsomega.2c04832
ACS Omega 2022, 7, 35951−35960

distribution of particle sizes were determined using a DLS particle analyzer (Otsuka Electronics, Shiga, Japan). The chemical surface of the RR-AuNPs was examined using FT-IR (PerkinElmer, Waltham, MA, USA) at wavelengths of 500−4000 cm^{-1}.

5.4. Evaluation of Intracellular Uptake and Cytotoxic Effect of RR-AuNPs. HaCaT human keratinocytes (CLS GmbH, Eppelheim, Germany) were maintained in Dulbecco's modified Eagle's medium (DMEM; Gibco, Grand Island, NY, USA) supplemented with 10% fetal bovine serum (Gibco) and 100 U penicillin/100 μg/mL streptomycin (Gibco) in a humidified incubator with 5% CO_2/95% air. The cells were added to a 96-well plate (SPL Life Sciences, Pocheon, Korea) at a density of 1×10^4 cells/well. After stabilization for 24 h, the medium was replaced with serum-free DMEM containing various concentrations of RR-AuNPs. Intracellular uptake and localization of RR-AuNPs were confirmed using a TIRS microscopy system equipped with DIC at 1 and 3 h. TIRS microscopy was performed using an upright Olympus BX51 microscope (Olympus Optical Co., Ltd., Tokyo, Japan). The equipment of DIC included a polarizer, beam-splitting modified Wollaston prism, beam-recombining modified Wollaston prism, and analyzer above a polished dove prism. The illumination light was provided by a 100 W halogen lamp. All images were obtained using MetaMorph 7.5 software (Universal Imaging, Sunnyvale, CA, USA). The cytotoxic effect of RR-AuNPs was evaluated at 24 h after RR-AuNP treatment using an MTT (Sigma) method according to a previous report[49] and live/dead cell staining assay (Invitrogen, Carlsbad, CA, USA) using a fluorescence microscope (Leica Microsystems, Wetzlar, Germany) according to the manufacturer's recommendations.

5.5. *In Vitro* Atopic Dermatitis Model Using HaCaT Cells. HaCaT cells were plated in 6-well plates (SPL Life Sciences) at a density of 2×10^5 cells/well. After stabilization for 24 h, the medium was changed to serum-free DMEM containing treatments for 1 h, and a recombinant protein mixture containing 10 ng/mL TNF-α (210-TA-100/CF; R&D Systems, Minneapolis, MN, USA) and 10 IFN-γ (285-IF-100/CF; R&D Systems) (T + I) was added to the cells to generate an in vitro inflammation model.

5.6. ROS Detection. After T + I stimulation for 24 h, ROS was detected using an ROS detection assay kit (ab139476; Abcam, Cambridge, UK) and a fluorescence microscope (Leica Microsystems) according to the manufacturer's recommendations.

5.7. Quantitative Real-time PCR. After T + I stimulation for 24 h, the cells were rinsed twice with phosphate-buffered saline (PBS; pH 7.2). Total RNA extraction, reverse transcription of RNA into cDNA, and quantitative real-time PCR (qRT-PCR) were performed as described previously.[50] The sequences of the gene-specific primers (Macrogen, Seoul, Korea) are listed in Table S1.

5.8. ELISA and Western Blotting. After T + I stimulation for 24 h, the cell culture supernatant was collected to quantify inflammatory cytokines according to the manufacturer's recommendations. Detailed information on the quantitative ELISA kits used in this study is provided in Table S2. The cells were rinsed twice with PBS and extracted using RIPA lysis buffer (Thermo Fisher Scientific, Waltham, MA, USA) containing protease inhibitors (GenDEPOT, Katy, TX, USA). The collected proteins were normalized using a bicinchoninic acid protein assay kit (Thermo Fisher Scientific), separated on a 10% sodium dodecyl sulfate-polyacrylamide gel, and transferred to a polyvinylidene fluoride membrane (Thermo Fisher Scientific) according to a previously described method.[50] Western blotting was used to evaluate NF-κB and MAPK signaling molecules as previously reported.[51] The antibodies used in this study are listed in Table S3, which were detected using a chemiluminescent imaging system (WSE-6370 LuminoGraph III Lite; ATTA, Tokyo, Japan) and quantified using ImageJ software (https://imagej.nih.gov/ij/; NIH, Bethesda, MD, USA).

5.9. Statistical Analysis. All experiments were performed in triplicate, and the data are expressed as the mean ± standard deviation. Student's *t*-test was used for statistical comparison between two groups, and the results were considered significant at $p < 0.05$, $p < 0.01$, and $p < 0.001$.

■ ASSOCIATED CONTENT

Supporting Information

The Supporting Information is available free of charge at https://pubs.acs.org/doi/10.1021/acsomega.2c04832.

Stability of the RR-AuNPs, real-time PCR primers used in this study, the information of the ELISA kits used in this study, and the information of the antibodies used in this study (PDF)

■ AUTHOR INFORMATION

Corresponding Authors

Hoon Kim − *Department of Food and Nutrition, Chung Ang University, Anseong 17546, Republic of Korea*; Phone: +82-31-888-6180; Email: saphead1106@hanmail.net

Yeon-Ju Kim − *Graduate School of Biotechnology, and College of Life Science, Kyung Hee University, Yongin 17104, Republic of Korea*; orcid.org/0000-0002-3474-066X; Phone: +82-31-201-2645; Email: yeonjukim@khu.ac.kr

Authors

Rongbo Wang − *Graduate School of Biotechnology, and College of Life Science, Kyung Hee University, Yongin 17104, Republic of Korea*

Sung-Kwon Moon − *Department of Food and Nutrition, Chung Ang University, Anseong 17546, Republic of Korea*

Woo-Jung Kim − *Biocenter, Gyeonggido Business and Science Accelerator, Suwon 16229, Republic of Korea*

Sanjeevram Dhandapani − *Graduate School of Biotechnology, and College of Life Science, Kyung Hee University, Yongin 17104, Republic of Korea*

Complete contact information is available at: https://pubs.acs.org/10.1021/acsomega.2c04832

Notes

The authors declare no competing financial interest.

■ ACKNOWLEDGMENTS

This work was carried out with KDBIO Corp. and supported by the fund "Cooperative Research Program for Agriculture Science and Technology Development (Project No.PJ01703502)" Rural Development Administration, Republic of Korea. This work was also supported by the Priority Research Centers Program through the National Research Foundation of Korea (NRF) funded by the Ministry of Education (2018R1A6A1A03025159) and Basic Science Research Program (2019R1I1A1A01061083) through the NRF.

REFERENCES

(1) Kobayashi, T.; Naik, S.; Nagao, K. Choreographing immunity in the skin epithelial barrier. *Immunity* **2019**, *50*, 552−565.
(2) Nguyen, A. V.; Soulika, A. M. The dynamics of the skin's immune system. *Int. J. Mol. Sci.* **2019**, *20*, 1811.
(3) Juráňová, J.; Franková, J.; Ulrichová, J. The role of keratinocytes in inflammation. *J. Appl. Biomed.* **2017**, *15*, 169−179.
(4) Albanesi, C.; Pastore, S. Pathobiology of chronic inflammatory skin diseases: interplay between keratinocytes and immune cells as a target for anti-inflammatory drugs. *Curr. Drug Metab.* **2010**, *11*, 210−227.
(5) Carretero, M.; Guerrero-Aspizua, S.; Illera, N.; Galvez, V.; Navarro, M.; García-García, F.; Dopazo, J.; Jorcano, J. L.; Larcher, F.; del Rio, M. Differential features between chronic skin inflammatory diseases revealed in skin-humanized psoriasis and atopic dermatitis mouse models. *J. Invest. Dermatol.* **2016**, *136*, 136−145.
(6) Chieosilapatham, P.; Kiatsurayanon, C.; Umehara, Y.; Trujillo-Paez, J.; Peng, G.; Yue, H.; Nguyen, L.; Niyonsaba, F. Keratinocytes: Innate immune cells in atopic dermatitis. *Clin. Exp. Immunol.* **2021**, *204*, 296−309.
(7) Aranez, V.; Ambrus, J. Immunologic adverse effects of biologics for the treatment of atopy. *Clin. Rev. Allergy Immunol.* **2020**, *59*, 220−230.
(8) Liu, D.; Ahmet, A.; Ward, L.; Krishnamoorthy, P.; Mandelcorn, E. D.; Leigh, R.; Brown, J. P.; Cohen, A.; Kim, H. A practical guide to the monitoring and management of the complications of systemic corticosteroid therapy. *Allergy Asthma Clin. Immunol.* **2013**, *9*, 30.
(9) Ahn, S.; Singh, P.; Castro-Aceituno, V.; Yesmin Simu, S.; Kim, Y.-J.; Mathiyalagan, R.; Yang, D.-C. Gold nanoparticles synthesized using Panax ginseng leaves suppress inflammatory-mediators production via blockade of NF-κB activation in macrophages. *Artif. Cells, Nanomed. Biotechnol.* **2017**, *45*, 270−276.
(10) Xu, X. Y.; Tran, T. H. M.; Perumalsamy, H.; Sanjeevram, D.; Kim, Y.-J. Biosynthetic gold nanoparticles of Hibiscus syriacus L. callus potentiates anti-inflammation efficacy via an autophagy-dependent mechanism. *Mater. Sci. Eng. C* **2021**, *124*, 112035.
(11) Abdel-Mottaleb, M. M.; Try, C.; Pellequer, Y.; Lamprecht, A. Nanomedicine strategies for targeting skin inflammation. *Nanomedicine* **2014**, *9*, 1727−1743.
(12) Ramos Campos, E. V.; Proença, P. L. D. F.; Doretto-Silva, L.; Andrade-Oliveira, V.; Fraceto, L. F.; de Araujo, D. R. Trends in nanoformulations for atopic dermatitis treatment. *Expert Opin. Drug Deliv.* **2020**, *17*, 1615−1630.
(13) Ghosalkar, S.; Singh, P.; Ravikumar, P. Emerging topical drug delivery approaches for the treatment of Atopic dermatitis. *J. Cosmet. Dermatol.* **2022**, *21*, 536−549.
(14) Krishnaswamy, K.; Vali, H.; Orsat, V. Value-adding to grape waste: Green synthesis of gold nanoparticles. *J. Food Eng.* **2014**, *142*, 210−220.
(15) Mittal, A. K.; Chisti, Y.; Banerjee, U. C. Synthesis of metallic nanoparticles using plant extracts. *Biotechnol. Adv.* **2013**, *31*, 346−356.
(16) Shah, M.; Fawcett, D.; Sharma, S.; Tripathy, S. K.; Poinern, G. E. J. Green synthesis of metallic nanoparticles via biological entities. *Materials* **2015**, *8*, 7278−7308.
(17) Ochir, S.; Park, B.; Nishizawa, M.; Kanazawa, T.; Funaki, M.; Yamagishi, T. Simultaneous determination of hydrolysable tannins in the petals of Rosa rugosa and allied plants. *J. Nat. Med.* **2010**, *64*, 383−387.
(18) Ng, T.; He, J.; Niu, S.; Zhao, Z.; Pi, W.; Shao, F.; Liu, L. A gallic acid derivative and polysaccharides with antioxidative activity from rose (Rosa rugosa) flowers. *J. Pharm. Pharmacol.* **2004**, *56*, 537−545.
(19) Um, M.; Han, T.-H.; Lee, J.-W. Ultrasound-assisted extraction and antioxidant activity of phenolic and flavonoid compounds and ascorbic acid from rugosa rose (Rosa rugosa Thunb.) fruit. *Food Sci. Biotechnol.* **2018**, *27*, 375−382.
(20) Tursun, X.; Zhao, Y.; alat, Z.; Xin, X.; AdilaTursun, R.; Abdulla, H.; AkberAisa, H. Anti-inflammatory effect of Rosa rugosa flower extract in lipopolysaccharide-stimulated RAW264. 7 macrophages. *Biomol. Ther.* **2016**, *24*, 184.
(21) Lee, Y.-H.; Jung, M. G.; Kang, H. B.; Choi, K.-C.; Haam, S.; Jun, W.; Kim, Y.-J.; Cho, H. Y.; Yoon, H.-G. Effect of anti-histone acetyltransferase activity from Rosa rugosa Thunb.(Rosaceae) extracts on androgen receptor-mediated transcriptional regulation. *J. Ethnopharmacol.* **2008**, *118*, 412−417.
(22) Xie, Y.; Zhang, W. Antihypertensive activity of Rosa rugosa Thunb. flowers: angiotensin I converting enzyme inhibitor. *J. Ethnopharmacol.* **2012**, *144*, 562−566.
(23) Dubey, S. P.; Lahtinen, M.; Sillanpää, M. Green synthesis and characterizations of silver and gold nanoparticles using leaf extract of Rosa rugosa. *Colloids Surf., A* **2010**, *364*, 34−41.
(24) Barabadi, H.; Honary, S.; Ebrahimi, P.; Mohammadi, M. A.; Alizadeh, A.; Naghibi, F. Microbial mediated preparation, characterization and optimization of gold nanoparticles. *Braz. J. Microbiol.* **2014**, *45*, 1493−1501.
(25) Wang, R.; Xu, X.; Puja, A. M.; Perumalsamy, H.; Balusamy, S. R.; Kim, H.; Kim, Y.-J. Gold Nanoparticles Prepared with Phyllanthus emblica Fruit Extract and Bifidobacterium animalis subsp. lactis Can Induce Apoptosis via Mitochondrial Impairment with Inhibition of Autophagy in the Human Gastric Carcinoma Cell Line AGS. *Nanomaterials* **2021**, *11*, 1260.
(26) Ali, S.; Bacha, M.; Shah, M. R.; Shah, W.; Kubra, K.; Khan, A.; Ahmad, M.; Latif, A.; Ali, M. Green synthesis of silver and gold nanoparticles using Crataegus oxyacantha extract and their urease inhibitory activities. *Biotechnol. Appl. Biochem.* **2021**, *68*, 992−1002.
(27) Das, R. K.; Gogoi, N.; Bora, U. Green synthesis of gold nanoparticles using Nyctanthes arbortristis flower extract. *Bioprocess Biosyst. Eng.* **2011**, *34*, 615−619.
(28) Ahmad, N.; Bhatnagar, S.; Saxena, R.; Iqbal, D.; Ghosh, A.; Dutta, R. Biosynthesis and characterization of gold nanoparticles: kinetics, in vitro and in vivo study. *Mater. Sci. Eng. C* **2017**, *78*, 553−564.
(29) Pozo, C.; Rodríguez-Llamazares, S.; Bouza, R.; Barral, L.; Castaño, J.; Müller, N.; Restrepo, I. Study of the structural order of native starch granules using combined FTIR and XRD analysis. *J. Polym. Res.* **2018**, *25*, 266.
(30) Faghihzadeh, F.; Anaya, N. M.; Schifman, L. A.; Oyanedel-Craver, V. Fourier transform infrared spectroscopy to assess molecular-level changes in microorganisms exposed to nanoparticles. *Nanotechnol. Environ. Eng.* **2016**, *1*, 1−16.
(31) Yang, J.-H.; Yoo, J.-M.; Lee, E.; Lee, B.; Cho, W.-K.; Park, K.-I.; Yeul Ma, J. Y. Anti-inflammatory effects of Perillae Herba ethanolic extract against TNF-α/IFN-γ-stimulated human keratinocyte HaCaT cells. *J. Ethnopharmacol.* **2018**, *211*, 217−223.
(32) Werfel, T. The role of leukocytes, keratinocytes, and allergen-specific IgE in the development of atopic dermatitis. *J. Invest. Dermatol.* **2009**, *129*, 1878−1891.
(33) Lim, H. S.; Jin, S. E.; Kim, O. S.; Shin, H. K.; Jeong, S. J. Alantolactone from Saussurea lappa Exerts Antiinflammatory Effects by Inhibiting Chemokine Production and STAT1 Phosphorylation in TNF-α and IFN-γ-induced in HaCaT cells. *Phytother. Res.* **2015**, *29*, 1088−1096.
(34) Morales, J.; Homey, B.; Vicari, A. P.; Hudak, S.; Oldham, E.; Hedrick, J.; Orozco, R.; Copeland, N. G.; Jenkins, N. A.; McEvoy, L. M.; Zlotnik, A. CTACK, a skin-associated chemokine that preferentially attracts skin-homing memory T cells. *Proc. Natl. Acad. Sci. U.S.A.* **1999**, *96*, 14470−14475.
(35) Wilmer, J.; Luster, M. Chemical induction of interleukin-8, a proinflammatory chemokine, in human epidermal keratinocyte cultures and its relation to cytogenetic toxicity. *Cell Biol. Toxicol.* **1995**, *11*, 37−50.
(36) Albanesi, C.; Scarponi, C.; Giustizieri, M. L.; Girolomoni, G. Keratinocytes in inflammatory skin diseases. *Curr. Drug Targets: Inflammation Allergy* **2005**, *4*, 329−334.
(37) Wang, Y.; Huo, J.; Zhang, D.; Hu, G.; Zhang, Y. Chemerin/ChemR23 axis triggers an inflammatory response in keratinocytes through ROS-sirt1-NF-κB signaling. *J. Cell. Biochem.* **2019**, *120*, 6459−6470.
(38) Yang, C.; Yang, Z.; Zhang, M.; Dong, Q.; Wang, X.; Lan, A.; Zeng, F.; Chen, P.; Wang, C.; Feng, J. Hydrogen sulfide protects against

https://doi.org/10.1021/acsomega.2c04832
ACS Omega 2022, 7, 35951−35960

chemical hypoxia-induced cytotoxicity and inflammation in HaCaT cells through inhibition of ROS/NF-κB/COX-2 pathway. *PLoS One* **2011**, *6*, No. e21971.
(39) Park, J.-H.; Kim, M.-S.; Jeong, G.-S.; Yoon, J. Xanthii fructus extract inhibits TNF-α/IFN-γ-induced Th2-chemokines production via blockade of NF-κB, STAT1 and p38-MAPK activation in human epidermal keratinocytes. *J. Ethnopharmacol.* **2015**, *171*, 85−93.
(40) Jung, M.-R.; Lee, T. H.; Bang, M.-H.; Kim, H.; Son, Y.; Chung, D. K.; Kim, J. Suppression of thymus-and activation-regulated chemokine (TARC/CCL17) production by 3-O-β-D-glucopyanosylspinasterol via blocking NF-κB and STAT1 signaling pathways in TNF-α and IFN-γ-induced HaCaT keratinocytes. *Biochem. Biophys. Res. Commun.* **2012**, *427*, 236−241.
(41) Yang, J.-H.; Hwang, Y.-H.; Gu, M.-J.; Cho, W.-K.; Ma, J. Y. Ethanol extracts of Sanguisorba officinalis L. suppress TNF-α/IFN-γ-induced pro-inflammatory chemokine production in HaCaT cells. *Phytomedicine* **2015**, *22*, 1262−1268.
(42) Lim, S. J.; Kim, M.; Randy, A.; Nam, E. J.; Nho, C. W. Effects of Hovenia dulcis Thunb. extract and methyl vanillate on atopic dermatitis-like skin lesions and TNF-α/IFN-γ-induced chemokines production in HaCaT cells. *J. Pharm. Pharmacol.* **2016**, *68*, 1465−1479.
(43) Khorasanizadeh, M.; Eskian, M.; Gelfand, E. W.; Rezaei, N. Mitogen-activated protein kinases as therapeutic targets for asthma. *Pharmacol. Ther.* **2017**, *174*, 112−126.
(44) Kaminska, B. MAPK signalling pathways as molecular targets for anti-inflammatory therapy—from molecular mechanisms to therapeutic benefits. *Biochim. Biophys. Acta* **2005**, *1754*, 253−262.
(45) Sur, B.; Kang, S.; Kim, M.; Oh, S. Alleviation of atopic dermatitis lesions by a benzylideneacetophenone derivative via the MAPK signaling pathway. *Inflammation* **2019**, *42*, 1093−1102.
(46) Caamaño, J.; Hunter, C. A. NF-kappaB family of transcription factors: central regulators of innate and adaptive immune functions. *Clin. Microbiol. Rev.* **2002**, *15*, 414−429.
(47) Liu, T.; Zhang, L.; Joo, D.; Sun, S.-C. NF-κB signaling in inflammation. *Signal Transduct. Target. Ther.* **2017**, *2*, 17023.
(48) Dhandapani, S.; Xu, X.; Wang, R.; Puja, A. M.; Kim, H.; Perumalsamy, H.; Balusamy, S. R.; Kim, Y.-J. Biosynthesis of gold nanoparticles using Nigella sativa and Curtobacterium proimmune K3 and evaluation of their anticancer activity. *Mater. Sci. Eng. C* **2021**, *127*, 112214.
(49) Kim, T. H.; Kim, W. J.; Park, S. Y.; Kim, H.; Chung, D. K. In vitro anti-wrinkle and skin-moisturizing effects of evening primrose (Oenothera biennis) sprout and identification of its active components. *Processes* **2021**, *9*, 145.
(50) Xu, X. Y.; Choi, H. S.; Park, S. Y.; Kim, J.-K.; Seo, K. H.; Kim, H.; Kim, Y.-J. Hibiscus syriacus L. cultivated in callus culture exerts cytotoxicity in colorectal cancer via Notch signaling-mediated cholesterol biosynthesis suppression. *Phytomedicine* **2022**, *95*, 153870.
(51) Shin, H. Y.; Hwang, K. C.; Mi, X. J.; Moon, S. K.; Kim, Y. J.; Kim, H. Rhamnogalacturonan I-rich polysaccharide isolated from fermented persimmon fruit increases macrophage-stimulatory activity by activating MAPK and NF-κB signaling. *J. Sci. Food Agric.* **2021**, *102*, 2846−2854.

https://doi.org/10.1021/acsomega.2c04832
ACS Omega 2022, 7, 35951−35960